Contents lists available at ScienceDirect

Applied Catalysis B: Environmental

Facile fabrication of RGO-WO$_3$ composites for effective visible light photocatalytic degradation of sulfamethoxazole

Wenyu Zhu [a,b], Faqian Sun [a], Ronn Goei [b], Yan Zhou [a,b,*]

[a] School of Civil and Environmental Engineering, Nanyang Technological University, 50 Nanyang Avenue, Singapore 639798, Republic of Singapore
[b] Nanyang Environment and Water Research Institute (NEWRI), 1 Cleantech Loop, CleanTech One, Singapore 637141, Republic of Singapore

ARTICLE INFO

ABSTRACT

The presence of various antibiotics in the aquatic systems has become one of the emerging environmental issues. Sulfonamides group is one of the most commonly used antibiotics which cannot be effectively removed by conventional treatment methods. This study aims to explore the degradation feasibility of sulfonamides by applying novel photocatalysts powered by visible light. Sulfamethoxazole (SMX), one of the most widely used sulfonamide class antibiotics was chosen as target pollutant to evaluate the photocatalytic degradation performance. Three types of reduced graphene oxide-WO$_3$ (RGO-WO$_3$) composites (RW-100, RW-200 and RW-400) as visible light driven photocatalysts were prepared via a facile one step hydrothermal method. Without pH adjustment, more than 98% removal of SMX was achieved within 3 hours by both RW-200 and RW-100 under visible light irradiation. The good photocatalytic activity of RGO-WO$_3$ composites demonstrates that they can be utilized as effective photocatalysts to degrade sulfonamide class of antibiotics. In addition, the photocatalytic intermediates of SMX were analyzed and the photodegradation pathway was proposed. RW-200 can be used for real application due to its high photocatalytic efficiency and excellent recyclability.

© 2017 Elsevier B.V. All rights reserved.

1. Introduction

Recently, the emergence of antibiotics and their residues in various aquatic systems has drawn wide attention due to their potential threat to both human health and aquatic ecosystems. As emerging persistent pollutants, though the concentration of antibiotics and their residues in the aquatic environment is usually low, they are believed to be able to raise antibiotic resistance in microorganisms in the long term [1]. Sulfonamides are one of the most extensively used antibiotics in human and veterinary medicine and large amount of sulfonamides finds their way into the environment every year [2–4].

Though sulfonamides are biodegradable, the biodegradation process is generally slow and not effective, therefore, conventional wastewater treatment plants (WWTPs) have limited removal ability towards sulfonamides [5,6]. Hence, it is necessary to develop more efficient treatment technologies to eliminate sulfonamides as well as other antibiotics. Many researchers are now turning their attention to application of advanced oxidation processes (AOPs) to remove trace micropollutants including antibiotics. Particularly, AOPs can be employed as complementary methods to conventional water treatment or as alternative strategies for industrial wastewater treatment. Among various AOPs, heterogenous photocatalysis driven by solar energy is demonstrated to be efficient, cost effective and environmental friendly, which make it a promising approach to remove trace micropollutants [5,7,8].

In comparison to widely studied TiO$_2$ with a wide band gap (around 3.2 eV) [9,10], n-type semiconductor Tungsten trioxide (WO$_3$) has a much narrower band gap of 2.4-2.8 eV which presents strong absorption of the solar spectrum[11]. Together with its other specific properties like nontoxicity, stable physicochemical properties, and good resistance to photocorrosion, WO$_3$ has been proposed to be an effective photocatalyst in degrading organic compound [11–15]. Nevertheless, the photocatalytic efficiency of pure WO$_3$ is limited by the slow charge transfer and the rapid recombination of photogenerated electron-hole pairs. To improve its photocatalytic performance, different methods such as morphology control, doping and synthesis of heterogeneous composites have been developed [15].

Graphene (GR) has unique two-dimensional (2D) structure, large surface area, excellent electronic and physicochemical properties [12,13,16–18]. GR and/or reduced graphene oxide (RGO)

* Corresponding author at: School of Civil and Environmental Engineering, Nanyang Technological University, 50 Nanyang Avenue, Singapore 639798, Republic of Singapore.
E-mail address: zhouyan@ntu.edu.sg (Y. Zhou).

are thereby regarded as excellent co-catalysts in constructing high performance heterogeneous photocatalysts [18–20]. They can work not only as superior supporting matrixes for bonding functional components but also excellent electron mediators to adjust electron transfer, and thus restrain the recombination of photogenerated charges and subsequently improve the electron-hole separation [10,18,21]. Together with the increased adsorption capacity for reactants, extended photoresponding range and enhanced visible light absorption intensity, graphene-based heterogeneous photocatalysts have shown improved photocatalytic activity.

To date, several researchers have reported the synthesis of WO_3-RGO composites as gas sensor [15,22–24], UV photodetector [25], photocatalysts [13–15,26,27] and oxygen evolution catalysts in PEC system [10,11,28–30]. However, it is still a challenge to synthesize uniform scattered WO_3 with good crystallinity, controlled morphology and particle sizes on RGO sheets [31]. Moreover, there has been no attempt to apply RGO-WO_3 composites to remove emerging pollutants like sulfonamides. Though several studies reported the use WO_3 as photocatalyst to degrade antibiotics, the addition of inorganic oxidants was usually required [32,33].

In this study, we report a facile one-step hydrothermal method to construct RGO-WO_3 composites with good crystallinity and small size 2D monoclinic-WO_3 (m-WO_3) nanoplates. It is supposed that compared to bare WO_3, the RGO-WO_3 composites would possess better photocatalytic performance as a result of the introduction of RGO sheets. In order to evaluate the photocatalytic activity of the as prepared composites, sulfamethoxazole (SMX), one of the commonly used sulfonamides antibiotics was chosen as target pollutant. According to the US Geological Survey, SMX is listed in the 30 most frequently detected wastewater contaminants with a long half-life of 85 to more than 100 days [34–36]. Since current WWTPs are insufficient at degrading SMX as well as other trace micropollutants, it is necessary to explore the possibility to apply photocatalytic process as an alternative strategy. Therefore, a systematic study has been conducted to investigate the photocatalytic properties of WO_3-RGO composites under visible light illumination towards SMX degradation without other additives.

2. Materials and methods

2.1. Materials

Natural graphite powder (LBG8010) was purchased from Superior Graphite (USA). Sulfuric acid (H_2SO_4, 95–98%), hydrochloric acid (HCl, 35%), potassium permanganate ($KMnO_4$), ethanol, sodium tungstate dihydrate ($Na_2WO_4 \cdot 2H_2O$), sodium nitrate ($NaNO_3$), isopropanol (IPA), benzoquinone (BQ) and sodium oxalate (SO) and sulfamethoxazole (SMX) were purchased from Sigma-Aldrich. Hydrogen peroxide (H_2O_2, 30%) was supplied by VWR. All chemicals were used as received and no further purification was needed.

2.2. Preparation of graphene oxide (GO)

GO was synthesized based on the modified Hummer's method [37,38]. In brief, 2.5 g natural graphite powders and 2.5 g $NaNO_3$ were firstly mixed by 120 mL concentrated H_2SO_4 in an ice bath. Then, 15 g $KMnO_4$ was divided into five equal parts and was slowly added into above slurry under continuous stirring. The mixture was then allowed to react at 35 °C for 6 h and after that 150 mL deionized water was carefully added to avoid boiling. The diluted solution was then kept at around 95 °C for 15 min and subsequently the suspension was poured into a beaker with 700 mL DI water. To purify the product, 60 mL H_2O_2 (30%) was added, and the obtained yel-

low solution was then washed by diluted HCl (10 wt%), dialyzed for one week and centrifuged with DI water until the pH of the supernatant was close to 7. Finally, the obtained GO was dried at 80 °C and grinded into powders for further usage.

2.3. Synthesis of reduce graphene oxide-tungstate trioxide composites (RGO-WO_3)

For the preparation of RGO-WO_3 composites, one-step hydrothermal method was developed. First, the as prepared graphene oxide was dispersed in DI water with the assistance of ultrasonicator forming a stable suspension with a concentration of 0.5 mg mL^{-1}. Then preset amount of $Na_2WO_4 \cdot 2H_2O$ (100 mg, 200 mg and 400 mg, respectively) were dissolved in 10 mL above GO suspension. 5 mL 35% HCl was then slowly added in the 10 mL mixture with continuous stirring. The suspension was transferred to a 45 mL Teflon-lined stainless steel autoclave to undergo a heating process for 8 h at 140 °C. After cooling down naturally, the sample was collected and washed with ethanol and DI water for several times before being dried by vacuum freeze drier. Pure WO_3 sample was prepared with the same method where $Na_2WO_4 \cdot 2H_2O$ was dissolved by DI water rather than GO suspension. The samples obtained were annealed at 300 °C for 30 min to further reduce the GO sheets. With different $Na_2WO_4 \cdot 2H_2O$ dosages, the three samples were named RW-100, RW-200, and RW-400 respectively.

2.4. Materials characterization

The crystal phases of the obtained products were characterized by X-ray powder diffraction (XRD) using a D8-Advacne Bruker-AXS diffractometer with Cu Kα irradiation operated at 40 kV and 30 mA. The morphologies and structures of the samples were observed by a field-emission scanning electron microscope (FESEM, JEOL 6340) and transmission electron microscopy (TEM) and high-resolution TEM (HRTEM) using a JEOL 2010 microscope operated at 200 kV. X-ray photoelectron spectra (XPS) were measured by a Kratos Axis Ultra Spectrometer with a monochromic Al Kα source at 1486.7 eV, a voltage of 15 kV and an emission current of 10 mA. UV–vis Spectra were obtained with a Scan UV–vis spectrophotometer (UV–vis Spectrometer 2501PC, Shimadzu). Photoluminescence (PL) emission spectra were recorded on a PerkinElmer LS 55 Fluorescence spectrometer at 325 nm. Raman Spectra were tested by a Renishaw inVia Raman microscope with the excitation wavelength of 514.5 nm.

2.5. Photocatalytic activity test for SMX degradation

Photocatalytic activity of pure WO_3 nanoplates and its WA composites was evaluated by degradation of SMX (10 mg L^{-1}) using a 1.5 AM solar simulator (NEWPORT, USA) with a 200 W Xe arc lamp. Dichroic mirrors were utilized to control wavebands in specific ranges 420–630 nm (visible light). To remove the UV residual, a polycarbonate filter was utilized. In a typical experimental procedure, 100 mg sample was firstly dispersed into 50 mL of DI water in the reaction vessel of 250 mL, and then mixed with 50 mL of 20 mg L^{-1} SMX solution and the final concentration was 10 mg L^{-1}. After that, the vessel was continuously stirred for 1 h in the dark to reach the adsorption equilibrium. The photocatalytic test was initiated by switching on the solar simulator. Sampling was carried out at various time intervals by drawing 3.0 mL of the aliquot from the reaction vessel. The samples were immediately filtered with 0.45 μm cellulose acetate syringe membrane filters. Filtered samples were analyzed by high performance liquid chromatography (HPLC) to determine the SMX concentration. Operating conditions of HPLC can be found in Supplementary Information. The total organic carbon (TOC) remaining in the solution was measured with
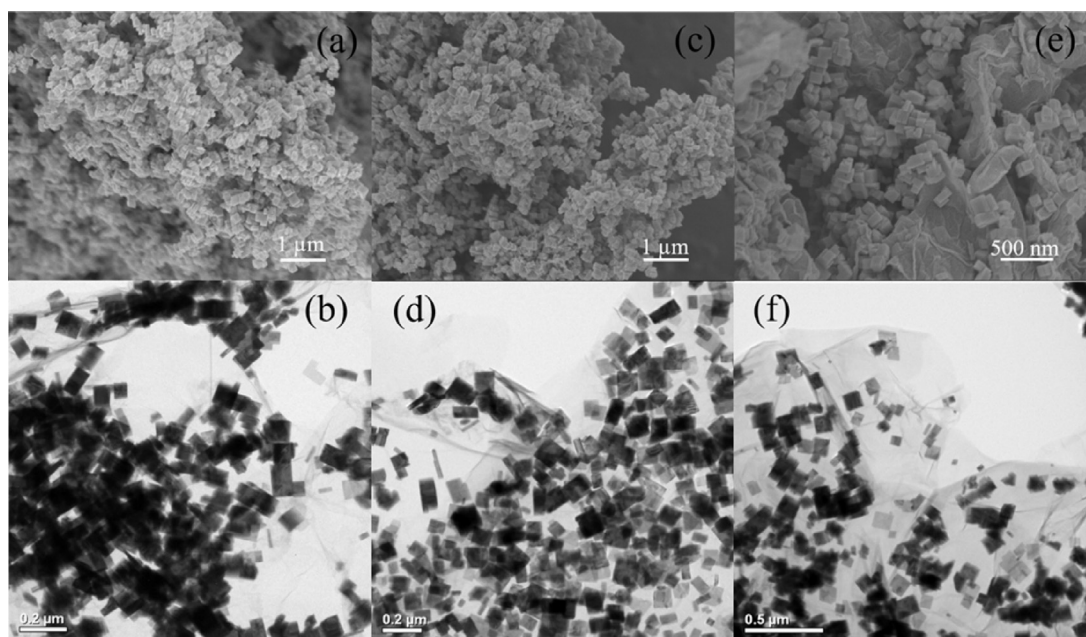
Fig. 1. FESEM and TEM images of RW-400 (a and b), RW-200 (c and d), and RW-100 (e and f).

a TOC analyzer (Analytikjena multi N/C 2100). The effect of initial pH (3.0, 5.2, 7.0 and 10.0) was studied and the pH was carefully adjusted with 0.1 M HCl and 0.2 M NaOH. The formation of various radicals in the photocatalytic process was investigated using SO, BQ and IPA as scavengers (0.5 mM). In addition, the degradation intermediates were detected by LC/MS/MS and the analysis method is illustrated in the Supplementary Information.

3. Results and discussion

3.1. Morphology and crystal structure characterization

Compared to the light yellow WO_3, the RGO-WO_3 composites had a gray color due to the introduction of RGO sheets and the sample color became darker with the increase of RGO amount (Fig. S1). The morphology of as-synthesized WO_3-RGO was observed by FESEM and TEM (Fig. 1). The WO_3 nanoplates formed on the RGO sheets had an average length of 150–200 nm. Due to the larger amount of WO_3 on the RGO sheets, aggregation could be found in RW-400 (Fig. 1(a) and (b)). By contrast, no obvious WO_3 aggregation was spotted from the TEM images of RW-200 and RW-100 (Fig. 1(d) and (f)) and the WO_3 nanoplates scattered uniformly on the RGO sheets. The lattice fringes of WO_3 on RGO was 0.376 nm (Fig. S3(e)) and was consistent with the (020) planes of m-WO_3. The TEM observation suggests that no significant lattice distortion occurred during the nucleation and growth of WO_3 on the RGO sheets.

The composition and crystallinity of the as prepared samples were firstly characterized with XRD (Fig. 2). The XRD pattern of pure WO_3 well followed the standard XRD pattern of m-WO_3 (PDF NO: 01-083-0951) [9,39]. The sharp peaks indicated the good crystallinity and no other peak was found revealing the high purity of WO_3 obtained. For RGO-WO_3 composites, the XRD patterns were quite similar to that of WO_3 except that a broad peak locating at around 25–30° were observed in the XRD pattern of RW-100. This broad peak was in agreement with the (002) planes originating from the graphitic layered structure [40]. More importantly, the distinguishing peak of GO at around 10° was not observed in the three RGO-WO_3 composites compared with the XRD pattern of GO (Fig. S4(a)), verifying that GO had been successfully reduced to RGO.
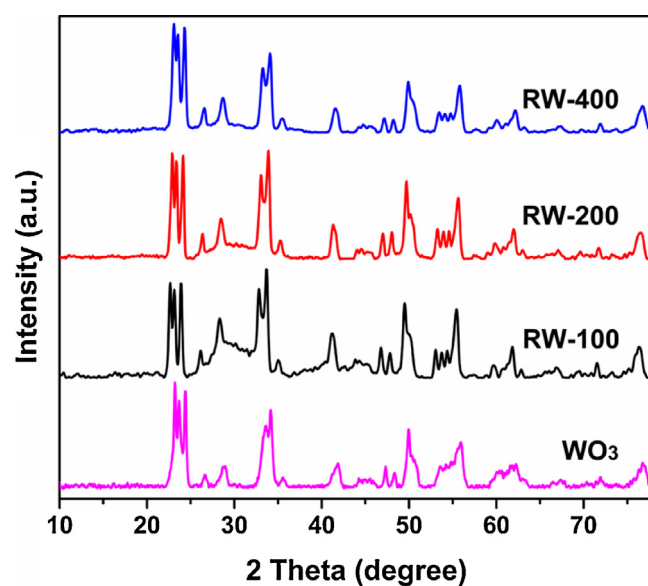

Fig. 2. Compartion of XRD patterns of WO_3, RW-100, RW-200 and RW 400.

The XRD results confirm that the introduction of RGO would not affect the growth of new crystal orientations of WO_3 where RGO sheets can work as a platform for WO_3 to nucleate and grow.

The phase structures of the obtained RGO-WO_3 composites were further explored by Raman spectra using WO_3 as control (Fig. 3(a)). Five typical peaks situating at 132, 268, 326, 714 and 808 cm^{-1} were detected in bare WO_3 belonging to the wavenumbers of m-WO_3. Particularly, the peak at 132 cm^{-1} was assigned to the lattice vibration of crystalline WO_3, while the peaks at around 268 cm^{-1} and 326 cm^{-1} were attributed to δ(O-W-O) bending mode [41]. The rest two peaks at 714 and 808 cm^{-1} were originated from the ν(O—W—O) vibrational stretching mode of the W-O-W bridging oxygen in the WO_6 octahedral units [42–46].

The Raman spectra of the three RGO-WO_3 composites were quite similar to that of WO_3 in the 100–850 cm^{-1} region. Slight shift could be observed in the RGO-WO_3 Raman spectra compared
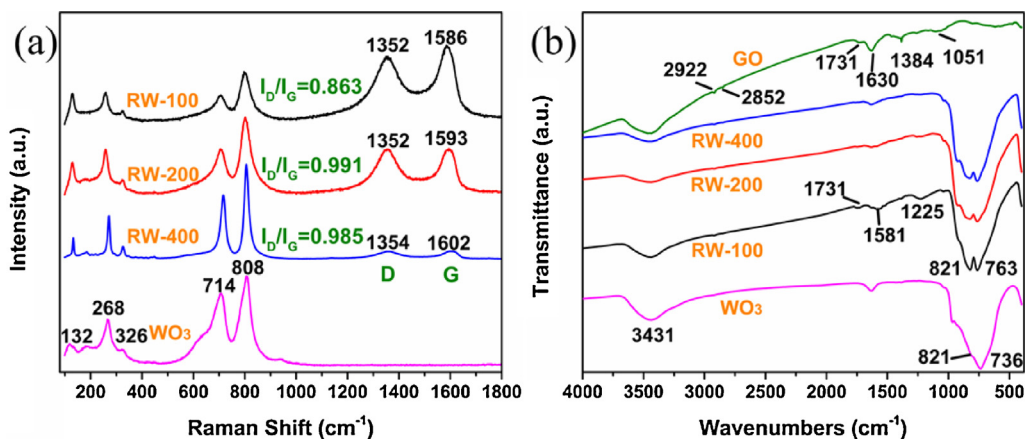
Fig. 3. Raman spectra of WO_3, RW-100, RW-200 and RW-400 (a); FTIR spectra of GO, WO_3, RW-100, RW-200 and RW-400 (b).

to that of bare WO_3. In particular, the vibrational stretching mode of $\nu(O-W-O)$ at $808\,cm^{-1}$ shifted to 805, 803 and $800\,cm^{-1}$ for RW-400, RW-200 and RW-100, respectively. Similar phenomena have been observed in previous studies as well [11,13,31], which may result from the strong interaction between RGO and WO_3. This implied that WO_3 nanoparticles were bonded to rather than physically adsorbed on RGO sheets. Moreover, two characteristic D (disorder carbon) and G (graphitic carbon) bands were detected in all three RGO-WO_3 composites, demonstrating the existence of RGO in the composites. The position of G band of RGO-WO_3 composites shifted up compared with that of GO (Fig. S4(b)) which could be ascribed to the superior interactions between WO_3 and RGO sheets [10]. The band intensity ratio (I_D/I_G) can be used to describe the degree of structural defects and a higher I_D/I_G is proposed to indicate a higher degree of structural defects [47,48]. Among three RGO-WO_3 composites, RW-200 had the highest I_D/I_G value (0.991) implying that RGO sheets in RW-200 contained more defects originated from incorporation such as formation of stronger or more interfacial interaction like $W-O-C$ band between WO_3 and RGO sheets [47]. This further confirms the removal of oxygen containing groups [49]. Moreover, such strong interaction will benefit the charge transfer between WO_3 and RGO once being irradiated [11,31].

The FTIR results are depicted in Fig. 3(b). The band at around $3431\,cm^{-1}$ was found in all five spectra which matched with the stretching vibration mode of $-OH$ and the physically adsorbed H_2O. In the FTIR spectrum of GO, characteristic absorption bands were observed at $1051\,cm^{-1}$ (C—O), $1225\,cm^{-1}$ (C—O—C), $1384\,cm^{-1}$ (C—OH), $1630\,cm^{-1}$ (C=C), and $1731\,cm^{-1}$ (C=O), respectively [10,27]. For bare WO_3, the board absorption in the range of $500-1000\,cm^{-1}$ were characteristic peaks of different O-W-O stretching vibrations in WO_3 crystal lattice [15,50]. In the FTIR spectra of three RGO-WO_3 composites, the characteristic bands of WO_3 still remained, at the same time bands originated from RGO could be found as well. In particular, the peak at $1225\,cm^{-1}$ (C—O—C) could be spotted in all three RGO-WO_3 composites, and the band at $1731\,cm^{-1}$ (C=O) was clearly detected in the spectrum of RW-100 though it was not significant enough to be observed in the RW-200 and RW-400 FTIR spectra due to the low RGO contents. Moreover, a new peak at $1581\,cm^{-1}$ corresponding to the aromatic skeletal C=C stretching vibration appeared, further proved the reduction of GO [51,52].

XPS was applied to study the element composition and valence state of the as prepared samples (Fig. 4). The overall XPS survey spectra of bare WO_3 and RGO-WO_3 composites confirmed the existence of element C, O and W (Fig. 4(a)) and no other impurity element was discovered implying the high purity of the samples.

From the high resolution spectra of W of WO_3, two peaks located at 38.1 and 35.9 eV representing the two characteristic W $4f_{7/2}$ and W4 $f_{5/2}$ peaks of W^{6+} in WO_3 were found (Fig. 4(b)) [11,23,53]. Slight shifts toward the higher binding energy of W $4f_{7/2}$ and W4 $f_{5/2}$ doublets in the RGO-WO_3 composites were observed which may be caused by the interaction between WO_3 and RGO sheets. For example, the peaks moved 0.2 eV to the higher binding energy for RW-200 compared to those of WO_3. Similar O 1s spectra were observed among three RGO-WO_3 samples (Fig. S6(a–c)), which could be de-convoluted to mainly three peaks. In the case of RW-200 (Fig. 4(d)), the de-convoluted O 1s spectra consisted three peaks that could be assigned to W-O (530.6 eV), C—O—C (532.3 eV) and O=C—O (533.6 eV). By contrast, the O 1s spectrum of WO_3 (Fig. S5(d)) could be only divided into two peaks, W-O peak at 530.1 eV and another peak at 531.9 eV due to the surface hydroxide (-OH) [54,55]. Thus, it is clear that the appearance of later two peaks in O 1s spectra of RGO-WO_3 composites was caused by RGO introduction. The C 1s spectrum of pristine GO (Fig. S5(c)) contained mainly four carbon bonds, including C—C/C=C (284.8 eV) originated from the graphitic sp^2 carbons; C—O—C (286.6 eV), C=O (287.1 eV), and O—C=O (288.8 eV) stemmed from oxygenate groups attached to the carbon atom [56,57]. According to the C 1s spectra, the C/O ratio of GO was calculated to be 0.884. The RGO-WO_3 samples showed similar C 1s spectra as shown in Fig. S6(d–f). Take RW-200 as an example (Fig. 4(c)), the mean peak of C 1s could be dissociated into three peaks: C—C/C=C at 284.8 eV, C—O—C at 286.5 eV and O—C=O at 288.7 eV, respectively. It is worth noting that the dominate peak found in RGO-WO_3 samples was C—C/C=C while the intensity of the peaks related to oxygenate functionalities (such as C—O—C and C=O) was much weaker than those of the GO. In addition, the C/O ratio obtained from the C 1s spectra of three RGO-WO_3 samples were 2.86, 3.03 and 2.97 for RW-100, RW-200 and RW-400, respectively. The weaker peaks originated from oxygenate groups and the higher C/O ratios indicate that a large number of oxygen containing groups were successfully removed.

3.2. Optical properties

Fig. 5(a) displays the UV–vis DRS spectra of WO_3 and three RGO-WO_3 composites. Bare WO_3 meanly presented light absorption in the UV range with the absorption on-set at 450 nm. By comparison, the RGO-WO_3 composites showed largely enhanced absorption in the visible light range (450–800 nm) resulted from RGO introduction as previously reported in other graphene-based composites [58,59]. Furthermore, the larger amount of RGO presented in the composites, the higher intensity could be achieved (RW-100 > RW-200 > RW-400). This enhanced visible light response could be
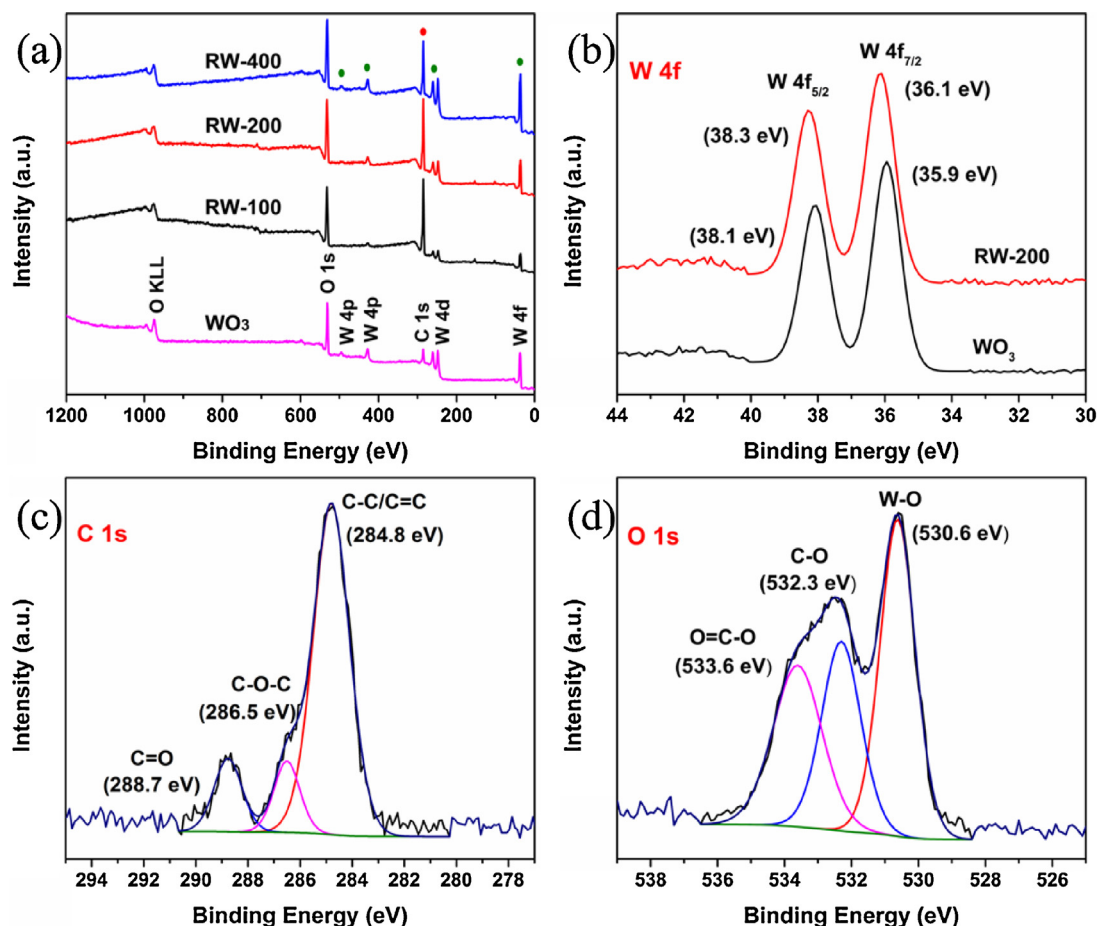
Fig. 4. XPS survey of WO_3, RW-100, RW-200 and RW-400 (a); High resolution XPS spectra of C 1 s for WO_3 and RW-200 (b), High resolution XPS spectra of O 1 s from RW-200 (c), and high resolution XPS spectra of O 1 s from RW-200.
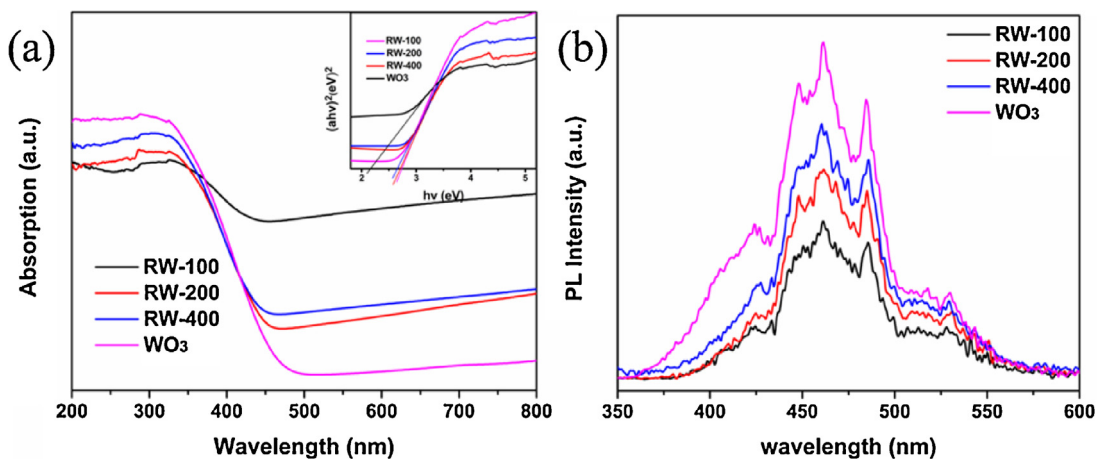

Fig. 5. UV–vis diffuse-reflectance spectra (DRS) of WO_3, RW-100, RW-200 and RW-400 (a), inset of (a) is the plots of $(\alpha h\nu)^2$ versus energy $h\nu$ of WO_3 and three RGO-WO_3 composites; Emission photoluminescence (PL) spectra of WO_3, RW-100, RW-200 and RW-400 with the excitation wavelength at 325 nm (b).

ascribed to two possible reasons: (1) the background light absorption of RGO in the visible light region, and (2) the enhanced surface electric charge of WO_3 due to the possible electronic transition of $\pi \rightarrow \pi^*$ of RGO and $n \rightarrow \pi^*$ between the n orbit of the oxygen species of WO_3 and RGO [11,60,61]. The band gaps were calculated by using modified Kubelka-Munk function as plot in the inset of Fig. 5(a). RW-100 had a band gap of 2.15 eV, while band gap of RW-200 and RW400 was 2.65 and 2.70 eV, respectively. Compared with bare WO_3 (2.75 eV), the band gaps of RGO-WO_3 composites were

remarkably narrowed which may come from the direct interaction between WO_3 and RGO sheets.

Fig. 5(b) illustrated the PL spectra of WO_3 and RGO-WO_3 samples. All four samples presented similar emission profile where mainly two peaks at around 461 nm and 480 nm could be observed. The stronger peak at 461 nm could be assigned to localized state in the band gap while the weaker one centered at 484 nm was attributed to the presence of oxygen vacancies or defects [54,62–66]. As revealed in Fig. 5(b), WO_3 displayed the highest
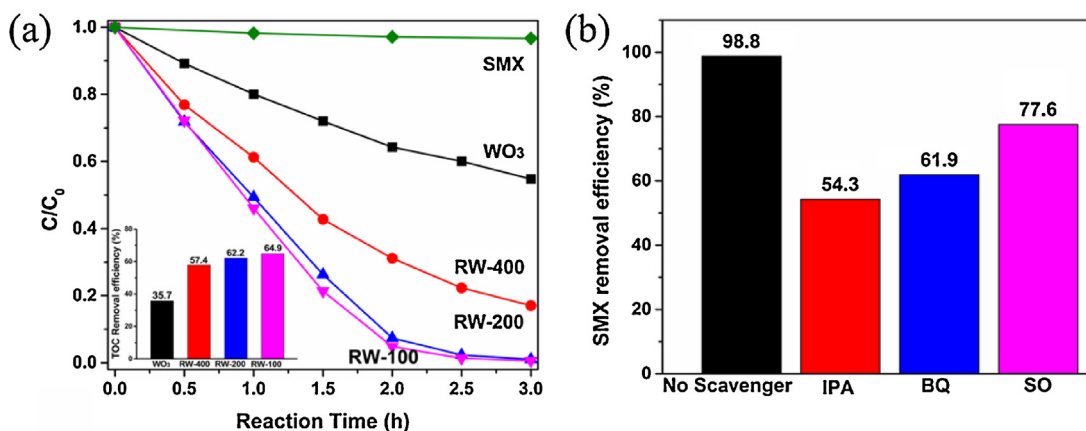
Fig. 6. Degradation of SMX under visible light over WO_3, RW-400, RW-200, RW-100 (a). Inset in (a) shows TOC removal efficiency of SMX with WO_3, RW-400, RW-200, RW-100 after 3 h reaction. Photocatalytic degradation performance of RW-200 in SMX removal with the presence of various scavengers after 3 h (b). Conditions: catalyst = 1.0 g L^{-1}, SMX = 10 mg L^{-1}, no pH adjustment.

PL intensity, while the peak intensities of three RGO-WO$_3$ were considerably diminished. Such quenched peak intensity indicates notably lower photogenerated electron-hole recombination rate in RGO-WO$_3$ composites. Accordingly, the electrons generated from light illumination can be more effectively separated and transferred where RGO sheets can act as an electron reservoir to accept and transfer electrons due to its better electron conductivity.

3.3. Photocatalytic activity of SMX

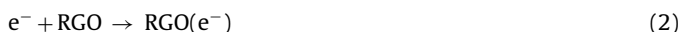#### 3.3.1. SMX degradation by various photocatalysts

The photocatalytic activity of the as prepared RGO-WO$_3$ composites was evaluated by the degradation of SMX under visible light illumination at room temperature and ambient pressure. Before applying visible light, SMX solution was continuously stirred for 3 h in dark without adding of any photocatalyst. No noticeable change of concentration was observed, demonstrating that the hydrolysis of SMX was negligible. Preliminary study found that the adsorption of SMX on all three RGO-WO$_3$ composites in dark was less than 8% indicating that the adsorption was not the main contributor to SMX removal (Fig. S7). The photodegradation of SMX without pH adjustment (about 5.2) over various catalysts is illustrated in Fig. 6(a). After 3 h visible light illumination without any catalyst, the concentration of SMX showed a very slight decrease (4.3%) while the degradation efficiency increased to 46.2% with the presence of WO$_3$. Better degradation efficiency was found by all RGO-WO$_3$ catalysts. Particularly, almost complete removal (>98%) of SMX was observed within 3 h when RW-200 and RW-100 were utilized. Meanwhile, as displayed in Fig. 6(a) inset, RGO-WO$_3$ composites showed higher TOC removal efficiency than that of WO$_3$. Generally, the TOC result was consistent with the degradation efficiency indicating the degree of mineralization towared SMX. In the case of SMX solution without adding catalyst, the TOC change was not clearly observed.

Though RW-100 showed slightly higher (0.4%) SMX removal efficiency than RW-200, its poor recyclability due to low density and poorer dispersion in the reaction system hinder its application in real situation. By contrast, RW-200 displayed not only comparable photocatalytic activity to RW-100 but also good recyclability (Fig. S8), making it a better candidate in practical application. Though slight loss of efficiency was found, this could be assigned to the unavoidable catalyst loss during the recovery process after each reaction cycle. Subsequently, RW-200 was applied in the following studies.

3.3.2. Mechanism for SMX photodegradtion

According to the above results, RGO-WO$_3$ composites possessed significantly enhanced photocatalytic performance in degrading SMX under visible light irradiation. Such improvement could be assigned to three possible reasons. Firstly, the UV–vis DRS spectra confirmed that the introduction of RGO could effectually narrow the band gap of WO$_3$ and subsequently extend its light response range to visible light range [67]. Meanwhile, RGO could act as electron trap and hence the photogenerated electrons could be transferred to the RGO sheets leading to the efficient electron-hole separation as verified by the suppressed PL spectra [68]. Additionally, RGO sheets with a large surface area could work as a supporter to provide adequate adsorption sites as well as catalytic sites during the photocatalytic reaction [18,69].

The possible mechanism of SMX degradation by RGO-WO$_3$ composites is portrayed in Fig. 7. When irradiated by visible light, WO$_3$ will absorb the incident photons generating electrons and holes. The excited electrons can transfer from Conduction band (CB) of WO$_3$ to RGO sheets which own a lower Fermi level ($E_F = -4.26$ eV) [59,68] and a better electrical conductivity (Eqs. (1) and (2)). After that, the photogenerated electrons will be scavenged by dissolved oxygen (O$_2$) in water resulting in effective electron-hole separation (Eq. (3)) producing $\bullet$O$_2^-$ [70]. These $\bullet$O$_2^-$ will then turn to HOO$\bullet$ which will combine with the trapped electrons to generate H$_2$O$_2$, and finally to produce OH$\bullet$ radicals (Eq. (4)–(6)) [71]. Simultaneously, the holes left on the Valence band (VB) of WO$_3$ can react with water and/or surface hydroxyl ($-$OH) to form hydroxyl radicals ($\bullet$OH) (Eqs. (7) and (8)). After a series of reactions, the radicals generated attack SMX in the close vicinity resulting in the degradation and mineralization of SMX (Eq. (9)).

$$WO_3 + h\nu \rightarrow WO_3(e^- + h^+) \tag{1}$$

$$e^- + RGO \rightarrow RGO(e^-) \tag{2}$$

$$RGO(e^-) + O_2 \rightarrow RGO + \bullet O^{2-} \tag{3}$$

$$O_2^- \bullet + H^+ \rightarrow HOO\bullet \tag{4}$$

$$HOO\bullet + e^- + H^+ \rightarrow H_2O_2 \tag{5}$$

$$H_2O_2 + e^- + \rightarrow OH\bullet + OH^- \tag{6}$$

$$H_2O + h^+ \rightarrow OH\bullet + H^+ \tag{7}$$

$$h^+ + OH^- \rightarrow \bullet OH \tag{8}$$

$$\bullet OH + SMX \rightarrow \text{degradation products} + CO_2, H_2O \tag{9}$$

To study the role of various radicals during the photocatalytic process, SO, IPA and BQ acting as h$^+$, OH$^-\bullet$ and O$_2^-\bullet$ scavengers
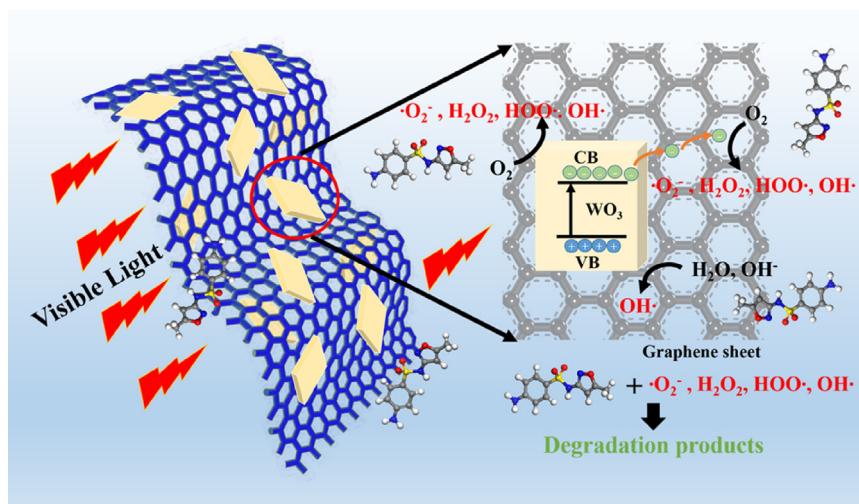
Fig. 7. Schematic illustration of the proposed mechanism for the enhanced degradation of SMX by RGO-WO$_3$ composites under visible light irradiation.

were added as depicted in Fig. 6(b). Generally, the presence of BQ and IPA remarkably inhibited the degradation of SMX under visible light while the inhibition effect caused by SO was less significant. Such results illustrate that O$_2^{-\bullet}$ and OH$^\bullet$ were the two primary radicals generated by RW-200 that involved in the photocatalytic degradation of SMX under visible light irradiation while h$^+$ played a minor role.

3.3.3. Parametric optimization study: effect of pH and catalyst dosage

To optimize the photocatalytic performance, the effect of two most important parameters affecting SMX photodegradation, namely pH and catalyst dosage were investigated (Fig. 7(a) and (b)) using RW-200 as photocatalyst. The reaction kinetics were estimated by fitting the data into the pseudo-first-order rate constant (See in the Supplementary information).

At initial pH 7.0, the removal rate of SMX was comparable to the efficiency achieved without pH adjustment. However, the degradation efficiency of SMX declined remarkably when initial pH was 3 and 10. As revealed by the strongly suppressed k values (Fig. 8(a) inset), pH can be considered as one of the most important factors affecting the photocatalytic process of RGO-WO$_3$ composites since it may influence (1) the electrostatic interaction between the photocatalysts and targeted organic pollutants; (2) the dispersion of photocatalysts in the reaction system.

The pH$_{pzc}$, which means that net zero charge, of RW-200 was estimated to be 2.46 (Fig. S2). The surface activity of RW-200 can be affected by pH as verified in the preliminary study where particle agglomerations and quick precipitation occurred when pH was decreased to 2.46. Therefore, when pH was 3, which was close to pH$_{pzc}$, the poor dispersion and formation of particle agglomerations would strongly hinder the photocatalytic process. When pH was risen to a higher value, the proportion of negatively charged RW-200 increased. At pH 7.0, most SMX existed in deprotonated form (Scheme 1) and thereafter the repulsive force between negatively charged surface of RW-200 and the negatively charged SMX would inhibit the adsorption of SMX onto the catalyst surface, leading to a slightly drop of the degradation rate. Similarly, the stronger repulsive force would further hinder the SMX removal efficiently at pH 10.

The effect of catalyst loading was revealed in Fig. 8(b) and it shows that increasing of catalyst dosage expedited SMX removal efficiency as confirmed by the k values where the highest value was achieved at dosage 1.0 g L^{-1}. Increase of catalyst loading would sup-

ply more available active sites for photocatalytic reactions as well as abundant effective surface area for adsorption process. Nevertheless, when the catalyst dosage was further increased to 2.0 g L^{-1}, slight reduction of SMX degradation rate was found which may be ascribed to the poorer light penetration in to the reaction system.

From the above study, it can be deduced that circumnuetral or slight acidic pH would be beneficial to SMX degradation by RGO-WO$_3$ composites under visible light. Therefore, no further adjustment of pH is required in real application.

3.3.4. Proposed degradation pathway

To explore the intermediate products and photodegradation pathway of SMX, LC/MS/MS was utilized. In the ES ($-$) mode (Fig. S10), peaks at m/z 286.1, 269.1, 268.2, 253.2, 252.2, 212.1, 196.1, 172.2, and 156.1 were detected. The peak at m/z 252.2 was referred to the deprotonated ion of SMX (Mw 253) and the appearance of peak at m/z 253.2 (C6, Mw 254) could be caused by the substitution of amino group (-NH$_2$) by hydroxyl group (-OH) as a result of ·OH attack. The peak at m/z 268.2 was in consistent with mono-hydroxylated derivatives (C1 and/or C4, Mw 269) stemming from addition of an ·OH radical to the SMX structure at different positions. These mono-hydroxylated compounds could be further oxidized where −NH$_2$ was replaced by −OH as verified by the appearance of peak at m/z 269.1 (C2 and/or C3, Mw 270). Moreover, a di-hydroxylated compound (C5, Mw 287) was found at m/z 286.1 which could be ascribed to the ·OH attack on the double bond of the isoxazole ring. Subsequently, radical attack was able to open the isoxazole ring and generate C9 (m/z 196.1, Mw 197) [2] while the observation of m/z 212.1 (C10, Mw 213) could be attributed to the attachment of ·OH radical on benzene ring of C5. Another possibility is that the following radical attack to C4 could result in isoxazole ring open which would give rise to the appearance of C7, the other tautomeric form of C5 [72]. C7 can be subsequently transformed to C8 (tautomeric of C9) as a result of radical attack on the aniline ring.

The peaks identified at m/z 156.1 (C11, Mw 157) indicates the cleavage of S-N bond as reported previously [2,3,5,73], and the rise of peak at m/z 172.2 (Mw 173) implies the appearance of sulfanilic acid (C13) and/or hydroxyl substituted sulfanilic acid (C14). Different from previous reports, C12 with a molecular weight of 98 that originated from the opening of the isoxazole ring was not identified in this study. However, degradation compound with a molecular weight of 99 (C15, m/z 100.1) was observed in the ES (+) mode (Fig. S11) which may result from the substitution of −NH$_2$ by
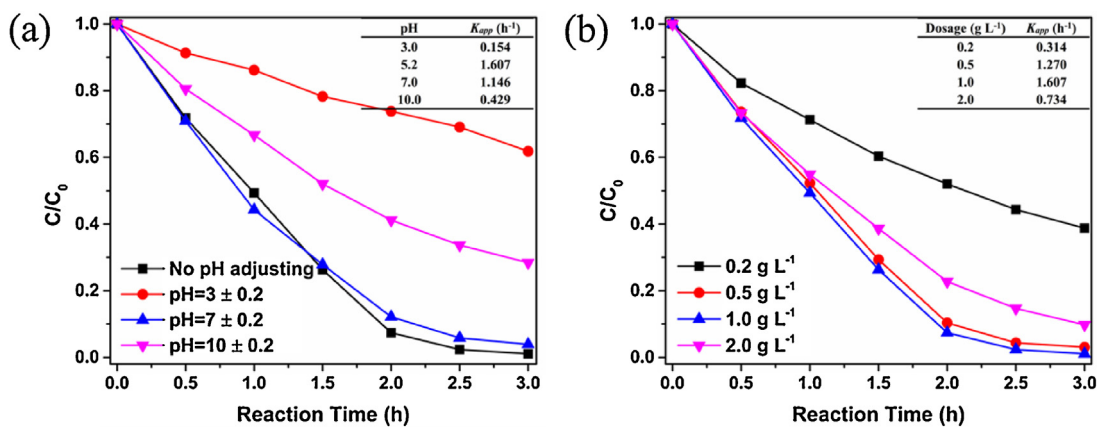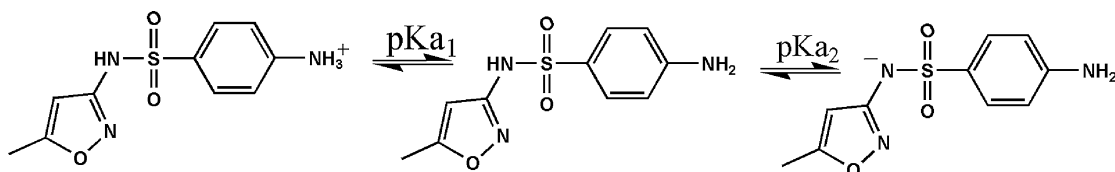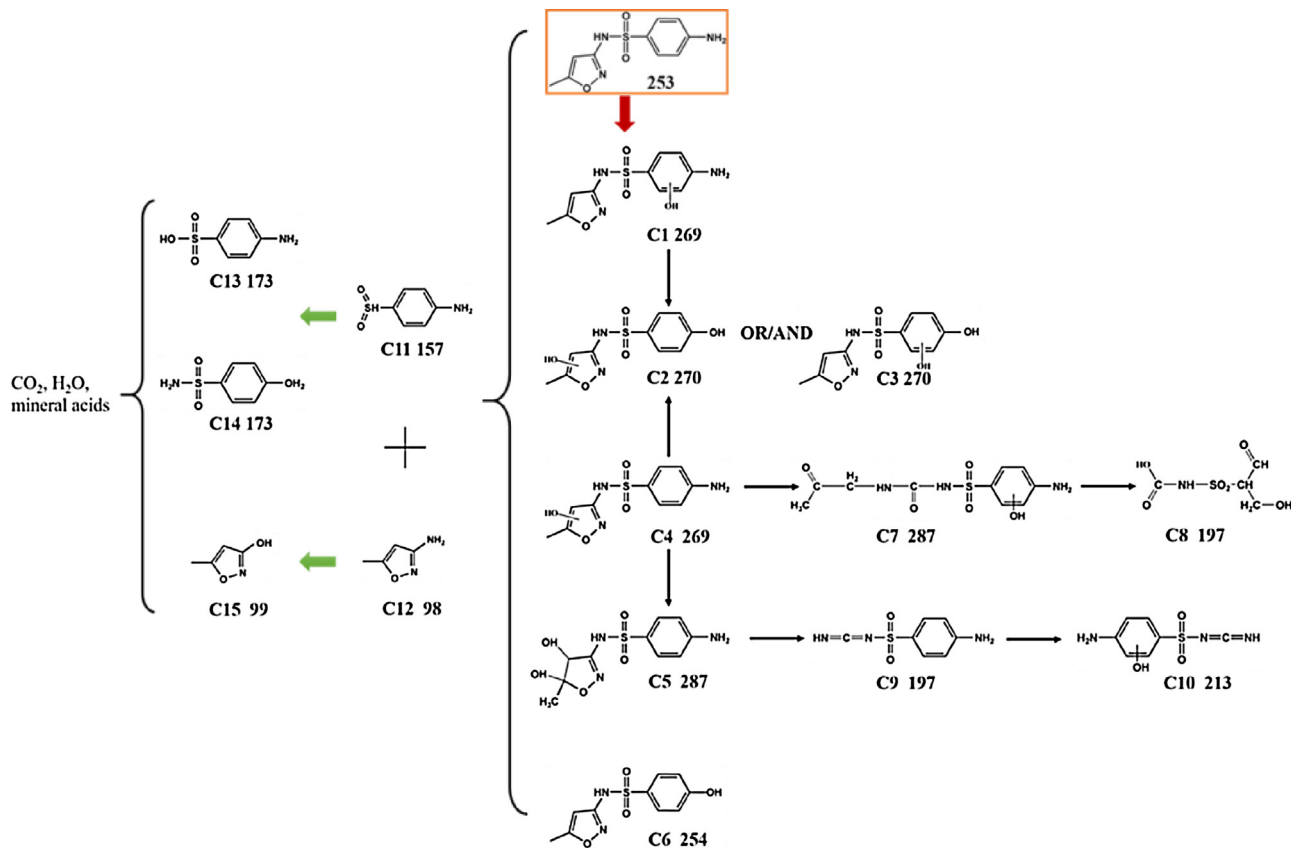
Fig. 8. Degradation of SMX under visible light by RW-200 at various pH (a). Condition: catalyst = 1.0 g L^{-1}, SMX = 10 mg L^{-1}. Degradation of SMX under visible light by RW-200 at different catalyst dosages (b). Conditions: SMX = 10 mg L^{-1}, no adjustment of pH.

Scheme 1. The SMX structures at different pH values: pK_{a1} = 1.7 and pK_{a2} = 5.6.

Scheme 2. Proposed pathway for SMX photocatalytic degradation by RGO-WO$_3$ composites.

−OH. Eventually, the aniline and isoxazole rings opened by radical attack and all the organic intermediates would be further mineralized to CO$_2$ and H$_2$O under visible light illumination. On the basis of the detected intermediates, a degradation pathway of SMX is pro-

posed in Scheme 2 including: (1) ·OH attack (hydroxylation) on the benzene ring or isoxazole ring with the formation of mono- or di-hydroxyl derivatives of SMX; (2) cleavage of the S-N bond; (3) bond

cleavage of the benzene ring and isoxazole ring and (4) oxidation and mineralization of the organic intermediates.

4. Conclusions

In brief, a facile one step hydrothermal method was developed to synthesize RGO-WO$_3$ composites with good photostability and recyclability. Compared with pure WO$_3$, all three RGO-WO$_3$ composites showed significantly improved photocatalytic activity under visible light. The following conclusions can be drawn from this study:

a RW-200 showed excellent photocatalytic activity and good dispersion, making it a more competitive candidate among the three as-prepared RGO-WO$_3$ composites.
b Catalyst dosage has a significant impact on the photocatalytic activity. The best SMX removal efficiency was achieved when RW-200 loading was $1.0\,g\,L^{-1}$.
c SMX photodegradation over RW-200 can be significantly influenced by pH, where the near-neutral conditions showed the best process.

Current study provides a low-cost and simple method to fabricate RGO-WO$_3$ composites, and such RGO-WO$_3$ composites can be regarded as potential photocatalysts for environmental purification of organic pollutants.

Acknowledgements

Appendix A. Supplementary data

Supplementary data associated with this article can be found, in the online version, at http://dx.doi.org/10.1016/j.apcatb.2017.02.012.

References

[1] F. Bonvin, J. Omlin, R. Rutler, W.B. Schweizer, P.J. Alaimo, T.J. Strathmann, K. McNeill, T. Kohn, Direct photolysis of human metabolites of the antibiotic sulfamethoxazole: evidence for abiotic back-transformation, Environ. Sci. Technol. 47 (2013) 6746–6755.
[2] A.G. Trovo, R.F. Nogueira, A. Aguera, A.R. Fernandez-Alba, C. Sirtori, S. Malato, Degradation of sulfamethoxazole in water by solar photo-Fenton. Chemical and toxicological evaluation, Water Res. 43 (2009) 3922–3931.
[3] X. Liu, X. Zhang, K. Shao, C. Lin, C. Li, F. Ge, Y. Dong, Fe0-activated persulfate-assisted mechanochemical destruction of expired compound sulfamethoxazole tablets, RSC Adv. 6 (2016) 20938–20948.
[4] Y. Ji, C. Ferronato, A. Salvador, X. Yang, J.M. Chovelon, Degradation of ciprofloxacin and sulfamethoxazole by ferrous-activated persulfate: implications for remediation of groundwater contaminated by antibiotics, Sci. Total Environ. 472 (2014) 800–808.
[5] L. Hu, P.M. Flanders, P.L. Miller, T.J. Strathmann, Oxidation of sulfamethoxazole and related antimicrobial agents by TiO2 photocatalysis, Water Res. 41 (2007) 2612–2626.
[6] L. Wang, Y. Wu, Y. Zheng, L. Liu, F. Zhao, Efficient degradation of sulfamethoxazole and the response of microbial communities in microbial fuel cells, RSC Adv. 5 (2015) 56430–56437.
[7] M.R. Hoffmann, S.T. Martin, W. Choi, D.W. Bahnemann, Environmental applications of semiconductor photocatalysis, Chem. Rev. 95 (1995) 69–96.
[8] M. Dlugosz, P. Zmudzki, A. Kwiecien, K. Szczubialka, J. Krzek, M. Nowakowska, Photocatalytic degradation of sulfamethoxazole in aqueous solution using a floating TiO2-expanded perlite photocatalyst, J. Hazard. Mater. 298 (2015) 146–153.
[9] W. Zhu, J. Liu, S. Yu, Y. Zhou, X. Yan, Ag loaded WO3 nanoplates for efficient photocatalytic degradation of sulfanilamide and their bactericidal effect under visible light irradiation, J. Hazard. Mater. 318 (2016) 407–416.
[10] H. Huang, Z. Yue, G. Li, X. Wang, J. Huang, Y. Du, P. Yang, Ultraviolet-assisted preparation of mesoporous WO3/reduced graphene oxide composites: superior interfacial contacts and enhanced photocatalysis, J. Mater. Chem. A 1 (2013) 15110.
[11] B. Weng, J. Wu, N. Zhang, Y.J. Xu, Observing the role of graphene in boosting the two-electron reduction of oxygen in graphene-WO(3) nanorod photocatalysts, Langmuir 30 (2014) 5574–5584.
[12] H. Hajishafiee, P. Sangpour, N.S. Tabrizi, Facile synthesis and photocatalytic performance ofWO3/rGO nanocomposite for degradation of 1-naphthol, Nano 10 (2015) 1550072.
[13] L. Fu, T. Xia, Y. Zheng, J. Yang, A. Wang, Z. Wang, Preparation of WO3-reduced graphene oxide nanocomposites with enhanced photocatalytic property, Ceram. Int. 41 (2015) 5903–5908.
[14] P.-Q. Wang, Y. Bai, P.-Y. Luo, J.-Y. Liu, Graphene–WO3 nanobelt composite: elevated conduction band toward photocatalytic reduction of CO2 into hydrocarbon fuels, Catal. Commun. 38 (2013) 82–85.
[15] X. An, J.C. Yu, Y. Wang, Y. Hu, X. Yu, G. Zhang, WO3 nanorods/graphene nanocomposites for high-efficiency visible-light-driven photocatalysis and NO2 gas sensing, J. Mater. Chem. 22 (2012) 8525.
[16] F. Schedin, A. Geim, S. Morozov, E. Hill, P. Blake, M. Katsnelson, K. Novoselov, Detection of individual gas molecules adsorbed on graphene, Nat. Mater. 6 (2007) 652–655.
[17] A. Dato, V. Radmilovic, Z. Lee, J. Phillips, M. Frenklach, Substrate-free gas-phase synthesis of graphene sheets, Nano Lett. 8 (2008) 2012–2016.
[18] Q. Xiang, J. Yu, M. Jaroniec, Graphene-based semiconductor photocatalysts, Chem. Soc. Rev. 41 (2012) 782–796.
[19] N. Zhang, M.-Q. Yang, Z.-R. Tang, Y.-J. Xu, Toward improving the graphene?semiconductor composite photoactivity via the addition of metal ions as generic interfacial mediator, ACS Nano 8 (2013) 623–633.
[20] P.V. Kamat, Graphene-based nanoarchitectures. anchoring semiconductor and metal nanoparticles on a two-dimensional carbon support, J. Phys. Chem Lett. 1 (2010) 520–527.
[21] M.-Q. Yang, Y.-J. Xu, Selective photoredox using graphene-based composite photocatalysts, Phys. Chem. Chem. Phys. 15 (2013) 19102–19118.
[22] S. Srivastava, K. Jain, V.N. Singh, S. Singh, N. Vijayan, N. Dilawar, G. Gupta, T.D. Senguttuvan, Faster response of NO(2) sensing in graphene-WO(3) nanocomposites, Nanotechnology 23 (2012) 205501.
[23] A. Esfandiar, A. Irajizad, O. Akhavan, S. Ghasemi, M.R. Gholami, Pd–WO3/reduced graphene oxide hierarchical nanostructures as efficient hydrogen gas sensors, Int. J. Hydrogen Energy 39 (2014) 8169–8179.
[24] P.-G. Su, S.-L. Peng, Fabrication and NO2 gas-sensing properties of reduced graphene oxide/WO3 nanocomposite films, Talanta 132 (2015) 398–405.
[25] D. Shao, M. Yu, J. Lian, S. Sawyer, An ultraviolet photodetector fabricated from WO(3) nanodiscs/reduced graphene oxide composite material, Nanotechnology 24 (2013) 295701.
[26] S. Thangavel, M. Elayaperumal, G. Venugopal, Synthesis and properties of tungsten oxide and reduced graphene oxide nanocomposites, Mater. Express 2 (2012) 327–334.
[27] B. Chai, J. Li, Q. Xu, K. Dai, Facile synthesis of reduced graphene oxide/WO3 nanoplates composites with enhanced photocatalytic activity, Mater. Lett. 120 (2014) 177–181.
[28] J. Lin, P. Hu, Y. Zhang, M. Fan, Z. He, C.K. Ngaw, J.S.C. Loo, D. Liao, T.T.Y. Tan, Understanding the photoelectrochemical properties of a reduced graphene oxide–WO3 heterojunction photoanode for efficient solar-light-driven overall water splitting, RSC Adv. 3 (2013) 9330.
[29] H. Wu, M. Xu, P. Da, W. Li, D. Jia, G. Zheng, WO3-reduced graphene oxide composites with enhanced charge transfer for photoelectrochemical conversion, Phys. Chem. Chem. Phys. 15 (2013) 16138–16142.
[30] J. Qin, M. Cao, N. Li, C. Hu, Graphene-wrapped WO3 nanoparticles with improved performances in electrical conductivity and gas sensing properties, J. Mater. Chem. 21 (2011) 17167.
[31] J. Guo, Y. Li, S. Zhu, Z. Chen, Q. Liu, D. Zhang, W.-J. Moon, D.-M. Song, Synthesis of WO3@Graphene composite for enhanced photocatalytic oxygen evolution from water, RSC Adv. 2 (2012) 1356.
[32] H. Kim, H.-Y. Yoo, S. Hong, S. Lee, S. Lee, B.-S. Park, H. Park, C. Lee, J. Lee, Effects of inorganic oxidants on kinetics and mechanisms of WO3-mediated photocatalytic degradation, Appl. Catal. B: Environ. 162 (2015) 515–523.
[33] A. Rey, E. Mena, A.M. Chávez, F.J. Beltrán, F. Medina, Influence of structural properties on the activity of WO3 catalysts for visible light photocatalytic ozonation, Chem. Eng. Sci. 126 (2015) 80–90.
[34] L.A. Schaider, R.A. Rudel, J.M. Ackerman, S.C. Dunagan, J.G. Brody, Pharmaceuticals, perfluorosurfactants, and other organic wastewater compounds in public drinking water wells in a shallow sand and gravel aquifer, Sci. Total Environ. 468 (2014) 384–393.
[35] E. Kassotaki, G. Buttiglieri, L. Ferrando-Climent, I. Rodriguez-Roda, M. Pijuan, Enhanced sulfamethoxazole degradation through ammonia oxidizing bacteria co-metabolism and fate of transformation products, Water Res. 94 (2016) 111–119.
[36] J.O. Straub, Aquatic environmental risk assessment for human use of the old antibiotic sulfamethoxazole in Europe, Environ. Toxicol. Chem. (2015).
[37] W.S. Hummers Jr., R.E. Offeman, Preparation of graphitic oxide, J. Am. Chem. Soc. 80 (1958) 1339.

[38] X.-Z. Tang, C. Mu, W. Zhu, X. Yan, X. Hu, J. Yang, Flexible polyurethane composites prepared by incorporation of polyethylenimine-modified slightly reduced graphene oxide, Carbon 98 (2016) 432–440.

[39] T. Xiao, X.-Y. Wang, Z.-H. Zhao, L. Li, L. Zhang, H.-C. Yao, J.-S. Wang, Z.-J. Li, Highly sensitive and selective acetone sensor based on C-doped WO3 for potential diagnosis of diabetes mellitus, Sens. Actuators B 199 (2014) 210–219.

[40] Y.-X. Wang, S.-L. Chou, H.-K. Liu, S.-X. Dou, Reduced graphene oxide with superior cycling stability and rate capability for sodium storage, Carbon 57 (2013) 202–208.

[41] S. Bai, K. Zhang, J. Sun, D. Zhang, R. Luo, D. Li, C. Liu, Polythiophene-WO3 hybrid architectures for low-temperature H2S detection, Sens. Actuators B 197 (2014) 142–148.

[42] C. Santato, M. Odziemkowski, M. Ulmann, A. Jan, Crystallographically oriented mesoporous WO3 films: synthesis, characterization, and applications, J. Am. Chem. Soc. 123 (2001) 10639–10649.

[43] C.M. White, J.S. Jang, S.H. Lee, J. Pankow, A.C. Dillon, Photocatalytic activity and photoelectrochemical property of nano-WO[sub 3] powders made by hot-wire chemical vapor deposition, Electrochem. Solid State Lett. 13 (2010) B120.

[44] L. Xu, M.L. Yin, S. Frank Liu, Agx@WO3 core-shell nanostructure for LSP enhanced chemical sensors, Sci. Rep. 4 (2014) 6745.

[45] C.-Y. Su, H.-C. Lin, C.-K. Lin, Fabrication and optical properties of Ti-doped W[sub 18]O[sub 49] nanorods using a modified plasma-arc gas-condensation technique, J. Vac. Sci. Technol. B: Microelectron. Nanometer Struct. 27 (2009) 2170.

[46] M.F. Daniel, B. Desbat, J.C. Lassegues, B. Gerand, M. Figlarz, Infrared and Raman study of WO3 tungsten trioxides and WO3, xH2O tungsten trioxide tydrates, J. Solid State Chem. 67 (1987) 235–247.

[47] H. Yu, J. Tian, F. Chen, P. Wang, X. Wang, Synergistic effect of dual electron-cocatalysts for enhanced photocatalytic activity: rGO as electron-transfer mediator and Fe(III) as oxygen-reduction active site, Sci. Rep. 5 (2015) 13083.

[48] D. Luo, G. Zhang, J. Liu, X. Sun, Evaluation criteria for reduced graphene oxide, J. Phys. Chem. C 115 (2011) 11327–11335.

[49] P. Benjwal, M. Kumar, P. Chamoli, K.K. Kar, Enhanced photocatalytic degradation of methylene blue and adsorption of arsenic(iii) by reduced graphene oxide (rGO)–metal oxide (TiO2/Fe3O4) based nanocomposites, RSC Adv. 5 (2015) 73249–73260.

[50] S. Bai, K. Zhang, R. Luo, D. Li, A. Chen, C.C. Liu, Low-temperature hydrothermal synthesis of WO3 nanorods and their sensing properties for NO2, J. Mater. Chem. 22 (2012) 12643.

[51] Y. Chen, Z. Huang, H. Zhang, Y. Chen, Z. Cheng, Y. Zhong, Y. Ye, X. Lei, Synthesis of the graphene/nickel oxide composite and its electrochemical performance for supercapacitors, Int. J. Hydrogen Energy 39 (2014) 16171–16178.

[52] X. Liu, Z. Li, W. Zhao, C. Zhao, Y. Wang, Z. Lin, A facile route to the synthesis of reduced graphene oxide-wrapped octahedral Cu2O with enhanced photocatalytic and photovoltaic performance, J. Mater. Chem. A 3 (2015) 19148–19154.

[53] T. Zhang, Z. Zhu, H. Chen, Y. Bai, S. Xiao, X. Zheng, Q. Xue, S. Yang, Iron-doping-enhanced photoelectrochemical water splitting performance of nanostructured WO3: a combined experimental and theoretical study, Nanoscale 7 (2015) 2933–2940.

[54] L. Zhang, Y. Li, Q. Zhang, H. Wang, Hierarchical nanostructure of WO3 nanorods on TiO2 nanofibers and the enhanced visible light photocatalytic activity for degradation of organic pollutants, CrystEngComm 15 (2013) 5986.

[55] S.K. Park, H.J. Lee, M.H. Lee, H.S. Park, Hierarchically structured reduced graphene oxide/WO3 frameworks for an application into lithium ion battery anodes, Chem. Eng. J. 281 (2015) 724–729.

[56] J. Zhang, Z. Xiong, X.S. Zhao, Graphene–metal–oxide composites for the degradation of dyes under visible light irradiation, J. Mater. Chem. 21 (2011) 3634.

[57] N. Yang, J. Zhai, D. Wang, Y. Chen, L. Jiang, Two-dimensional graphene bridges enhanced photoinduced charge transport in dye-sensitized solar cells, Acs Nano 4 (2010) 887–894.

[58] F. Ning, M. Shao, S. Xu, Y. Fu, R. Zhang, M. Wei, D.G. Evans, X. Duan, TiO2/graphene/NiFe-layered double hydroxide nanorod array photoanodes for efficient photoelectrochemical water splitting, Energy Environ. Sci. 9 (2016) 2633–2643.

[59] M.S. Sher Shah, A.R. Park, K. Zhang, J.H. Park, P.J. Yoo, Green synthesis of biphasic TiO(2)-reduced graphene oxide nanocomposites with highly enhanced photocatalytic activity, ACS Appl. Mater. Interfaces 4 (2012) 3893–3901.

[60] Y. Ou, J. Lin, S. Fang, D. Liao, MWNT–TiO2:Ni composite catalyst: a new class of catalyst for photocatalytic H2 evolution from water under visible light illumination, Chem. Phys. Lett. 429 (2006) 199–203.

[61] T. Peng, P. Zeng, D. Ke, X. Liu, X. Zhang, Hydrothermal preparation of multiwalled carbon nanotubes (MWCNTs)/CdS nanocomposite and its efficient photocatalytic hydrogen production under visible light irradiation, Energy Fuels 25 (2011) 2203–2210.

[62] H. Katsumata, Y. Oda, S. Kaneco, T. Suzuki, Photocatalytic activity of Ag/CuO/WO3 under visible-light irradiation, RSC Adv. 3 (2013) 5028.

[63] M.T. Chang, L.J. Chou, Y.L. Chueh, Y.C. Lee, C.H. Hsieh, C.D. Chen, Y.W. Lan, L.J. Chen, Nitrogen-doped tungsten oxide nanowires: low-temperature synthesis on Si, and electrical optical, and field-emission properties, Small 3 (2007) 658–664.

[64] L. Tian, L. Ye, J. Liu, L. Zan, Solvothermal synthesis of CNTs–WO3 hybrid nanostructures with high photocatalytic activity under visible light, Catal. Commun. 17 (2012) 99–103.

[65] Q. -q. Jia, H. -m. Ji, P. Gao, X. Bai, Z. -g. Jin, Control of the acetone sensitive and selective properties of WO3 nanofibers by doping Co ions: effect of crystal symmetric structure on the responsivity of gas–solid boundaries for gas sensor, J. Mater. Sci. Mater. Electron. 26 (2015) 5792–5802.

[66] C.-Y. Su, H.-C. Lin, Direct route to tungsten oxide nanorod bundles: microstructures and electro-optical properties, J. Phys. Chem. C 113 (2009) 4042–4046.

[67] C. Chen, W. Cai, M. Long, B. Zhou, Y. Wu, D. Wu, Y. Feng, Synthesis of visible-light responsive graphene oxide/TiO2 composites with p/n heterojunction, Acs Nano 4 (2010) 6425–6432.

[68] P.V. Kamat, Graphene-based nanoassemblies for energy conversion, J. Phys. Chem Lett. 2 (2011) 242–251.

[69] Q. Xiang, J. Yu, Graphene-based photocatalysts for hydrogen generation, J. Phys. Chem Lett. 4 (2013) 753–759.

[70] W.Y. Teoh, J.A. Scott, R. Amal, Progress in heterogeneous photocatalysis: from classical radical chemistry to engineering nanomaterials and solar reactors, J. Phys. Chem Lett. 3 (2012) 629–639.

[71] T. Wu, G. Liu, J. Zhao, H. Hidaka, N. Serpone, Photoassisted degradation of dye pollutants. V. Self-photosensitized oxidative transformation of rhodamine B under visible light irradiation in aqueous TiO2 dispersions, J. Phys. Chem. B 102 (1998) 5845–5851.

[72] M.N. Abellán, B. Bayarri, J. Giménez, J. Costa, Photocatalytic degradation of sulfamethoxazole in aqueous suspension of TiO2, Appl. Catal. B: Environ. 74 (2007) 233–241.

[73] C. Qi, X. Liu, C. Lin, X. Zhang, J. Ma, H. Tan, W. Ye, Degradation of sulfamethoxazole by microwave-activated persulfate: kinetics, mechanism and acute toxicity, Chem. Eng. J. 249 (2014) 6–14.